



National Library
of Canada

Bibliothèque nationale
du Canada

Canadian Theses Service

Service des thèses canadiennes

Ottawa, Canada
K1A 0N4

NOTICE

The quality of this microform is heavily dependent upon the quality of the original thesis submitted for microfilming. Every effort has been made to ensure the highest quality of reproduction possible.

If pages are missing, contact the university which granted the degree.

Some pages may have indistinct print especially if the original pages were typed with a poor typewriter ribbon or if the university sent us an inferior photocopy.

Reproduction in full or in part of this microform is governed by the Canadian Copyright Act, R.S.C. 1970, c. C-30, and subsequent amendments.

AVIS

La qualité de cette microforme dépend grandement de la qualité de la thèse soumise au microfilmage. Nous avons tout fait pour assurer une qualité supérieure de reproduction.

S'il manque des pages, veuillez communiquer avec l'université qui a conféré le grade.

La qualité d'impression de certaines pages peut laisser à désirer, surtout si les pages originales ont été dactylographiées à l'aide d'un ruban usé ou si l'université nous a fait parvenir une photocopie de qualité inférieure.

La reproduction, même partielle, de cette microforme est soumise à la Loi canadienne sur le droit d'auteur, SRC 1970, c. C-30, et ses amendements subséquents.

Structure and Fluid Mechanics
of Starting Gas Jets

Mike Georgallis

A Thesis
in
The Department
of
Mechanical Engineering

Presented in Partial Fulfillment of the Requirements
for the Degree of Master of Engineering at
Concordia University
Montreal, Quebec, Canada

August 1989

© Mike Georgallis, 1989



National Library
of Canada

Bibliothèque nationale
du Canada

Canadian Theses Service Service des thèses canadiennes

Ottawa, Canada
K1A 0N4

The author has granted an irrevocable non-exclusive licence allowing the National Library of Canada to reproduce, loan, distribute or sell copies of his/her thesis by any means and in any form or format, making this thesis available to interested persons.

The author retains ownership of the copyright in his/her thesis. Neither the thesis nor substantial extracts from it may be printed or otherwise reproduced without his/her permission.

L'auteur a accordé une licence irrévocable et non exclusive permettant à la Bibliothèque nationale du Canada de reproduire, prêter, distribuer ou vendre des copies de sa thèse de quelque manière et sous quelque forme que ce soit pour mettre des exemplaires de cette thèse à la disposition des personnes intéressées.

L'auteur conserve la propriété du droit d'auteur qui protège sa thèse. Ni la thèse ni des extraits substantiels de celle-ci ne doivent être imprimés ou autrement reproduits sans son autorisation.

ISBN 0-315-51393-4

ABSTRACT

Structure and Fluid Mechanics of Starting Gas Jets

Mike Georgallis

Schlieren and light slicing visualization are used to study the structure of starting gas jets. The light slicing method, developed during the course of this study, permits observation of the inner structure of the starting jets involved. The available power used in the light slicing system is shown to be orders of magnitude above that of a laser system costing about the same. Some of the results were used to obtain quantitative data.

ACKNOWLEDGMENTS

The author thanks the Department of National Defence, whose contract supported most of the work presented here.

The author also thanks the Natural Sciences and Engineering Research Council of Canada for partial financial support for this work.

I would like to thank my graduate supervisor, Dr. A.J. Saber for giving me the freedom and opportunity to make critical decisions throughout the research work, yet educating me more than he or I realized.

I would also like to thank a number of colleagues who gave their time in group discussion and laboratory help. They are: Robert Cochrane, James Crone, Zhigang Fang, Pierre Gauthier, Peter Lawn, Tarik Wahab, and Boris Zelikin.

Finally, special thanks are directed toward Uzi Koren for the guidance he gave me in the laboratory at the early stages of the research.

TABLE OF CONTENTS

	Page
Title Page.	i
Signature Page.	ii
ABSTRACT.	iii
ACKNOWLEDGEMENTS.	iv
TABLE OF CONTENTS	v
LIST OF FIGURES	viii
LIST OF TABLES.	x
NOMENCLATURE.	xi
1.0 INTRODUCTION.	1
2.0 EXPERIMENTAL METHODS.	3
2.1 Optical Review	3
2.1.1 Imaging versus Point Sources.	3
2.1.2 Laser versus Flash Lamp Optics.	5
2.1.3 The Scheimpflug Rule.	6
2.1.4 The Cylindrical Lens.	7
2.2 Optical Systems.	8
2.2.1 Schlieren	8
2.2.2 Light Slicing	10
2.3 Optical Losses in the Flash Lamp System.	14
2.3.1 The Flash lamp.	14
2.3.2 Light Slicing Efficiency.	14
2.3.3 Available Power	17

	Page
2.4 Non-Optical Components	17
2.4.1 Shock Tube Design	17
2.4.2 Test Gases.	21
2.4.3 Electronics	21
2.4.4 Camera and Film	25
2.5 Accuracy of Systems.	27
2.6 Effect of Smoke.	29
3.0 EXPERIMENTAL RESULTS.	31
3.1 Data Reduction	31
3.2 Axial Results.	35
3.2.1 Schlieren	35
3.2.1.1 Helium Driving Air	35
3.2.1.2 Air Driving Air.	38
3.2.2 Light Slicing	41
3.2.2.1 Helium Driving Air + Smoke	42
3.2.2.2 Air Driving Air + Smoke.	45
3.2.3 Schlieren - Air Driving Air + Smoke	48
3.2.4 Quantitative Results.	51
3.3 Transverse Light Slicing Results	57
3.3.1 Air Driving Air + Smoke	58
3.4 Three-Dimensional Integration.	60

	Page
4.0 CONCLUDING REMARKS.	62
4.1 Future Work.	62
LIST OF REFERENCES.	64

LIST OF FIGURES

	Page
Fig. 2.1 : Rays Emitted from a Source	4
Fig. 2.2 : Scheimflug Rule.	6
Fig. 2.3 : Light Rays through a Cylindrical Lens.	7
Fig. 2.4 : Schlieren System	9
Fig. 2.5 : Light Slicing System	11
Fig. 2.6 : Experimental Setup of Light Slicing System	12
Fig. 2.7 : Shock Tube	18
Fig. 2.8 : 22 mm Diameter Shock Tube.	19
Fig. 2.9 : Driving and Injecting Smoke.	20
Fig. 2.10 : Instrumentation and Timing System.	22
Fig. 2.11 : Photograph of Instrumentation and Timing System	23
Fig. 2.12 : Delay Timer Block Diagram.	24
Fig. 2.13 : Flash Lamp Electronic Assembly	24
Fig. 2.14 : Photograph of Flash Lamp Electronic Assembly	25
Fig. 2.15 : Axial Light Slicing Setup.	26
Fig. 2.16 : Transverse Light Slicing Setup	26
Fig. 2.17 : Pressure Measurement Systems	28
Fig. 3.1 : Axial Light Slicing Results.	32
Fig. 3.2 : Scattering Angle Effect.	33
Fig. 3.3 : Axial Light Slicing Result with Data Reduction Grid	34
Fig. 3.4 : Schlieren - He driving Air	36

	Page
Fig. 3.5 :	Schlieren - Air driving Air. 39
Fig. 3.6 :	Light Slicing - He driving Air+Smoke . . 43
Fig. 3.7 :	Light Slicing - Air driving Air+Smoke. . 46
Fig. 3.8 :	Schlieren - Air driving Air+Smoke. . . . 49
Fig. 3.9 :	The Starting Jet 50
Fig. 3.10 :	Quantitative Measurements. 51
Fig. 3.11 :	Comparison of Primary Vortex Extent. . . 52
Fig. 3.12 :	Schlieren Data: Helium driving Air . . . 53
Fig. 3.13 :	Light Slicing Data: He driving Air+Smoke. 53
Fig. 3.14 :	Schlieren Data: Air driving Air. 55
Fig. 3.15 :	Light Slicing Data: Air driving Air+Smoke. 55
Fig. 3.16 :	Schlieren Data: Air Driving Air+Smoke. . 56
Fig. 3.17 :	Transverse Light Slicing Results: Air driving Air+Smoke. 59
Fig. 3.18 :	3-D Reconstruction of Starting Jet : Air driving Air+Smoke. 61

LIST OF TABLES

	Page
Table 2.1 : Location of Components in Schlieren System	10
Table 2.2 : Location of Components of the Light Slicing System	13
Table 2.3 : Optical Equipment for the Light Slicing System	13
Table 3.1 : Air Driving Air (Velocities in m/s). . .	56
Table 3.2 : He Driving Air (Velocities in m/s). . .	57

NOMENCLATURE

Chapter 2: EXPERIMENTAL METHODS

- R - spherical radius of light source
- δ - diameter of surface area of interest
- I - intensity
- I_0 - ideal intensity
- r - reflection efficiency
- n - index of refraction
- f - focal length

Chapter 3: EXPERIMENTAL RESULTS

- α - scattering angle
- f - focal length
- i - image distance
- o - object distance
- P_c - perpendicular object distance
- Q_c - perpendicular image distance
- M_c - magnification

1.0 INTRODUCTION

Jets are fluid exhaust flows, produced by a pressure drop across an orifice. A starting jet is the fluid in the region in the immediate neighborhood of the orifice, when the fluid is started from rest.

A paper by William Rogers published in 1858 shows sketches of visualization of a starting jet and of impulsively generated, single vortex rings [Ref. 1]. Later visualization work on vortex rings by Czermak in 1900 [Ref. 2] and Indra in 1901 [Ref. 3] also included sketches. These papers indicate the early appreciation of instabilities exhibited by vortex rings. Among the earliest photographs showing the growth of vortex rings in a circular jet are those of Johansen (1929), who investigated the circular jet produced downstream of a broad orifice plate set in a circular pipe [Ref. 4].

The starting jet has recently received research attention in two basic areas: First, in the understanding of the process by which they entrain surrounding fluid, and second, in the noise they produce. The investigations generally report jet flows with Reynolds numbers well below 500,000 and Mach numbers consistently low enough that the flows behave incompressibly. The fluid phenomena referred to as "coherent structures" have also received recent attention and their

behaviour is summarized in a 1986 review paper by Hussain [Ref. 5].

List, in 1982, cites evidence that the initial growth of jets is due to relatively large-scale motions generated at the jet boundaries [Ref. 6]. The evidence is accompanied by a description of the phenomena. "In the immediate neighborhood of the orifice, the high-speed jet flow causes a laminar shear layer to be produced. The shear layer is unstable and grows very rapidly, forming ring vortices that carry turbulent jet fluid into the irrotational ambient fluid and irrotational ambient fluid into the jet...". The vortex motion, he notes, develops a secondary circumferential instability that causes each vortex to break up. An understanding of these motions may be basic to an understanding of the physics of transition and turbulence phenomena.

In this work, flow visualization studies have been undertaken to observe the basic structure of starting gas jets.

2.0 EXPERIMENTAL METHODS

Schlieren and light slicing flow visualization techniques are used to study the starting jet. In this section, elements of the basic theory used to design the optical systems are presented. As part of the discussion, optical losses for the light slicing system are identified and the available luminous power produced is estimated. Given that the flash lamp spectrum is continuous, the luminous output is about four orders of magnitude above that of a laser system costing about the same.

2.1 Optical Review

Visualization requires conditioning of light rays to illuminate flow areas of interest. Such conditioning is achieved using optical elements such as lenses and mirrors. This section describes elements of the basic theory used to develop a light ray conditioning system.

2.1.1 Imaging versus Point Sources

Collimated light is needed for flash lamp light slicing. To produce collimated light from a point source, the source must be placed at the focal point of a converging lens.

However, obtaining collimated light from a finite image source is more difficult.

Consider Figure 2.1 which shows various light rays emitted from a source. The rays pass through lens L1, and intercept lens L2. It is evident that the larger the axial distance L, the smaller the angle with the optical axis that

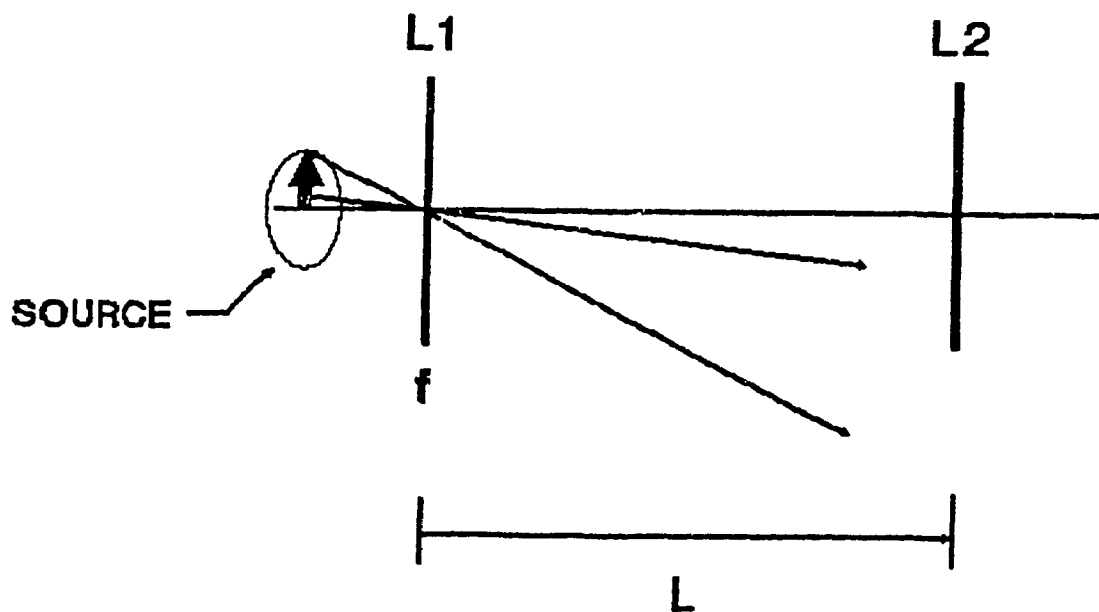


Figure 2.1: Rays Emitted from a Source

incident light rays make going toward lens L2. Thus, if lens L2 is to accept collimated light, it follows that L must be infinite. In practice, one is limited by the amount of space available in the work area.

To approach a collimated set of rays an optical stop or small diameter iris (much smaller than the object diameter) may also be placed in front of the object. This restricts the rays to those at a small angle with respect to the optical axis, simulating collimated light at later stages.

It is noted here, that large optical losses can result because of the space limitations and the use of the optical stops.

2.1.2 Laser versus Flash Lamp Optics

In contrast to a finite luminous source, a laser is capable of producing highly collimated light. This makes manipulation of the light rays straightforward permitting design of many optical systems. A drawback of such equipment is that high powered lasers, often required, are very expensive.

An alternative to employing a high powered laser is the flash lamp. However, because a flash lamp does not provide a point source of light, complications in optical arrangements result, as described in section 2.1.1. Furthermore, because the flash lamp arc's transparent enclosure reflects light in undesired directions, aspherical problems are present. These problems are reduced by selective use of irises within the

optical arrangement and thus high quality images can be produced.

2.1.3 The Scheimpflug Rule

When object planes are at angles other than perpendicular to the optical axis, the image plane has to be oriented to be in focus over the entire field. The relationship between the view plane and the image plane is described by the Scheimpflug rule of intersecting planes, namely "a subject plane is rendered sharply at full aperture when the three optical planes (subject plane, image plane and lens plane) intersect in a common line" [Ref. 7]. This relationship is illustrated in Figure 2.2. We note that the resulting image will not have a uniform magnification but will satisfy the thin lens formula.

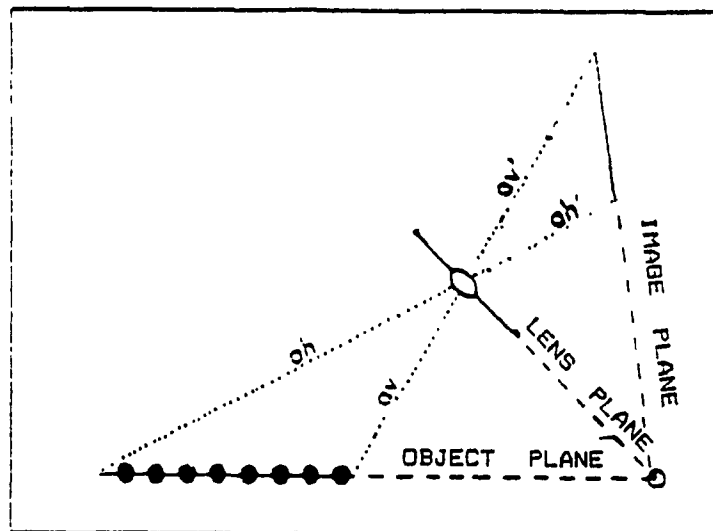


Figure 2.2 : Scheimpflug Rule

2.1.4 The Cylindrical Lens

Cylindrical lenses are used in the light slicing arrangement, to create a thin sheet of light. Figure 2.3 shows typical light rays passing through a cylindrical lens.

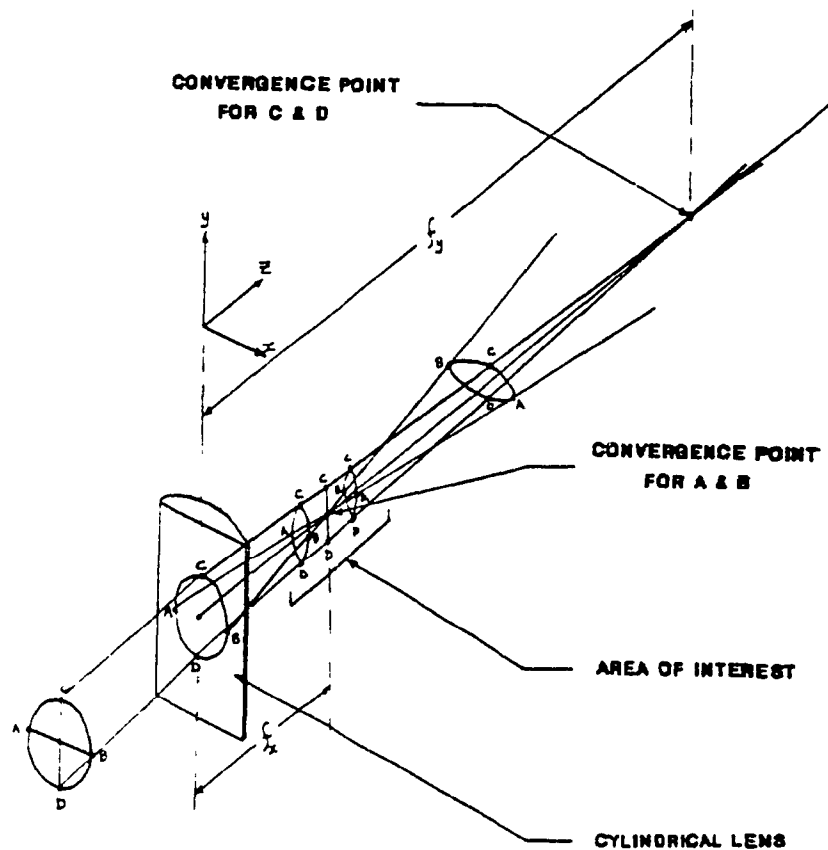


Figure 2.3 : Light Rays through a Cylindrical Lens

Focal length, f_x , defines the curvature of the lens in the x - z axis. Similarly, f_y , defines the curvature in the y - z axis (f_y is normally much larger than f_x). The area of interest occurs at the thin light slice created near focal length, f_x .

2.2 Optical Systems

This section describes the two optical systems that have been used in this study. These systems are schlieren and light slicing.

The source for both these systems is a high power flash lamp (EG&G 1P1 xenon flash lamp) rated to a maximum of 60 Joules. The flash lamp was chosen in order to provide sufficient illumination for photography. The lamp has a 1 mm nominal arc length. It is held by an EG&G "lite pac" flash lamp holder and is mounted on a 3 metre optical rail. The components of the flash lamp system are given in Reference 8. The pulse duration has been measured at approximately 1 μ s.

2.2.1 Schlieren

The schlieren system is shown in Figure 2.4. The figure shows the flash lamp light source at position 1. Light from the source is intersected by a parabolic mirror at position 2. When the flash lamp centre is located at the focal point of the mirror, the rays approaching the mirror are reflected in a parallel beam to position 4. The parallel beam intersects the flow area of interest at position 3.

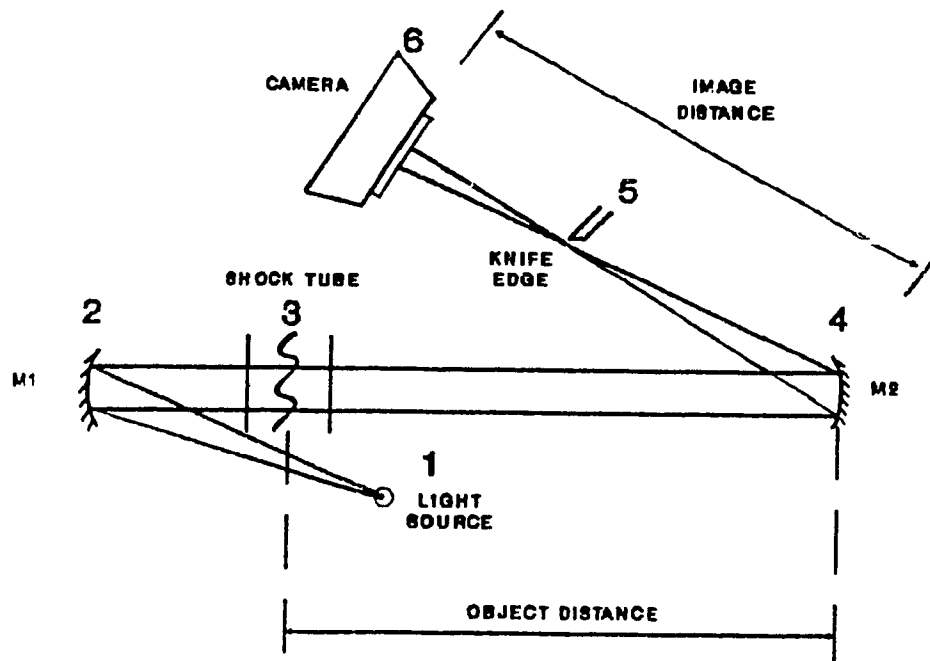


Figure 2.4 : Schlieren System

After passing through the test section, the light beam is reflected from a second parabolic mirror at position 4 to a focus at position 5. A knife edge is located at position 5 where only a fraction, usually $3/4$ of the incoming light, is permitted to pass. Rays that are deflected past the knife edge, as a result of changes in density of the flow, are imaged on a film focal plane at 6.

In practice, the angle between the axis of the incident and reflected light rays to the parabolic mirrors is minimized. This angle is set equal at both mirrors to avoid formation of elliptic cross-sections of the light ray.

Since the flash lamp is not a point source of light, a pinhole stop of 1/3 mm (0.013 inches) diameter is incorporated in the schlieren system. The pinhole is placed immediately in front of the light source, and is not shown in figure 2.4. The pinhole diminishes the size of the focal point at the knife edge, improving the acuity of the images. As a result crisper photographs have been taken. Table 2.1 gives the distances between components for the schlieren system. The overall size is about 3.0 m long by 1.5 m wide.

<u>REFERENCE PLANE</u>	<u>DISTANCE (METERS)</u>
1-2	1.22
2-3	0.91
3-4	3.05
4-5	1.22
5-6	0.81

Table 2.1 : Location of Components in Schlieren System

2.2.2 Light Slicing

Light slicing, also called planar imaging, is defined as "the creation of a light sheet that can illuminate a lamina of an optically thin system" [Ref. 9]. The lamina is suitable for illuminating a seeded, transparent fluid flow. The method permits observation of the inner structure of a starting submerged transient gas jet.

Various irises and lenses are suitably placed to create the optical system as shown in Figure 2.5. The figure shows the relative position of the components. Light emitted from

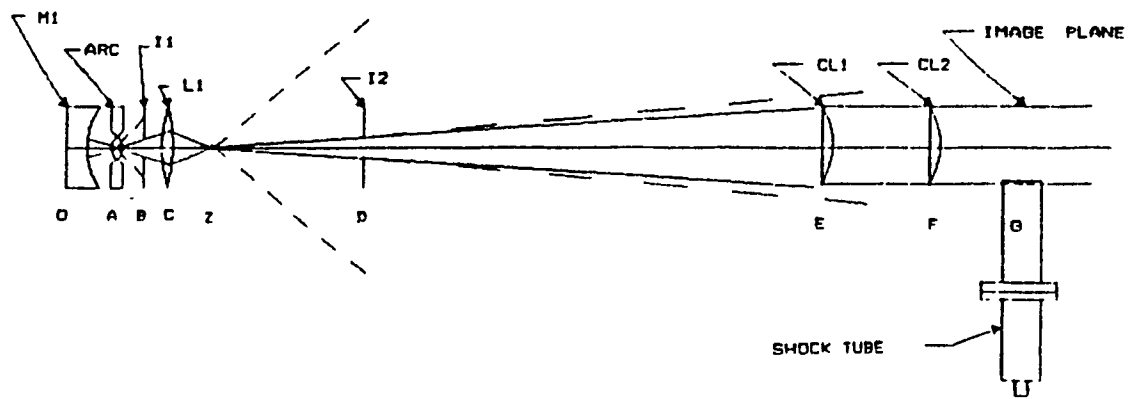


Figure 2.5 : Light Slicing System

the source at position A passes to iris I1 (position B) placed in front of the flashlamp. The iris removes light rays that would normally cause lens distortions at the periphery of lens L1 (position C). Mirror M1 (position O) is placed behind the source, effectively doubling the efficiency of the system. Lens L1 is actually a multiple camera lens system of effective focal length 75mm and an f-number of 1.9. It was found that a camera lens resolves the problem of chromatic aberrations found in a simple converging lens.

The final design for the system diminishes optical problems such as spherical aberration, oblique aberration, coma, astigmatism, field curvature, lens distortion, and chromatic aberration. The experimental set-up is shown in Figure 2.6.

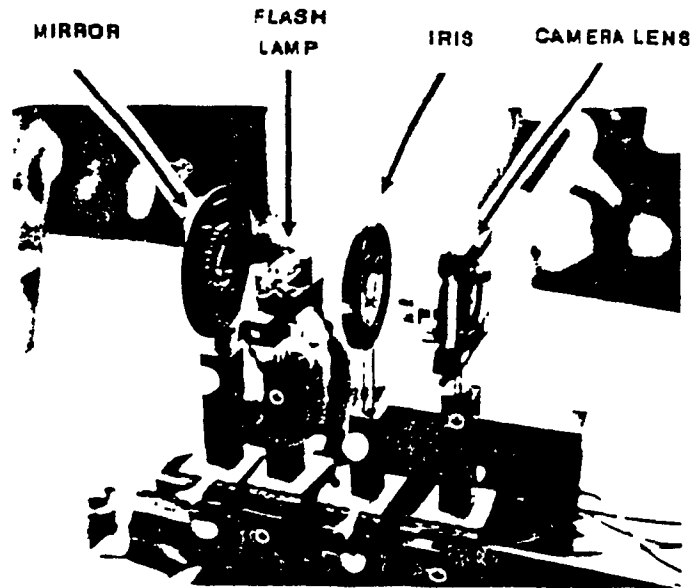


Figure 2.6 : Experimental Setup of Light Slicing System

Cylindrical lenses CL1 and CL2 (positions E and F respectively) were chosen to implement the required focal length for proper planar imaging of the jet scale. The distance between the cylindrical lens system and the source had to be as large as possible so that the lenses view the source as a point. Laboratory space limited this distance to approximately 1.5 meters.

Although iris I2 (position D) removes undesired light rays for CL1 and CL2, square irises had to be positioned just before both cylindrical lenses to tailor the edges for preventing lens distortions as in the case above. These irises are omitted in Figure 2.5.

Tables 2.2 and 2.3 give the distances between components, and the specifications of the various components, respectively.

<u>REFERENCE PLANE</u>	<u>DISTANCE (mm)</u>
OA	60
AB	70
BC	53
CD	410
DE	1050
EF	183
FG	406

Table 2.2 : Location of Components of the Light Slicing System

<u>NAME</u>	<u>DESCRIPTION</u>	<u>COMMENT</u>
M1	CONCAVE MIRROR	f=30 mm ; d=47.5
ARC	SHORT ARC FLASH LAMP	
I1	IRIS	d=18 mm
L1	CAMERA LENS	f=75 mm
I2	IRIS	d=30 mm
CL1	CYLINDRICAL LENS	} f=80mm;W=30mm } L=130mm
CL2	CYLINDRICAL LENS	

Table 2.3 : Optical Equipment for the Light Slicing System

2.3 Optical Losses in the Flash Lamp System

The flash-lamp light slicing system efficiency is assessed through the calculation of intensity ratios.

2.3.1 Flash Lamp Power

A total of 50 μF of capacitance charged to 1000 VDC, are used to power the flash lamp. This provides 25 Joules of energy. Assuming a luminous efficiency of 1%, for converting electrical energy into luminosity, [Ref. 10] 0.25 Joules of energy remain. This energy is released over a period of approximately 1 microsecond yielding a luminous power output of 250kW.

2.3.2 Light Slicing Efficiency

As mentioned above, the system efficiency is assessed through the calculation of intensity ratios. Intensity ratios are evaluated using the cross-sectional area ratios of the system elements.

There are four major contributions to intensity losses in the light slicing system of Figure 2.5. The first two are due to irises I1 and I2. The following two loss sections arise from the two cylindrical lenses.

To calculate the loss at each element, the light source is presumed concentrated over a sphere of radius R. A portion of the surface area on this sphere, in spherical coordinates, is given by;

$$A = R^2 \int_0^{2\pi} \int_{\cos^{-1}(\delta/2R)}^{\pi/2} \cos(\phi) \, d\phi \, d\theta \quad (2.1)$$

where δ , is the diameter of the surface area of interest.

The above integral becomes;

$$A = 2\pi R^2 [1 - \sqrt{1 - (\delta/2R)^2}] \quad (2.2)$$

and the intensity ratio is then equal to;

$$\left(\frac{I}{I_0} \right)_1 = [1 - \sqrt{1 - (\delta/2R)^2}] \quad (2.3)$$

If the surface area of interest in the light slicing system is located at iris I1 (position B) of Figure 2.5, $\delta=18\text{mm}$ and $R=70\text{mm}$, which yield an intensity ratio of 0.0166. Therefore 1.66% of the light passes through this stage of the system.

Similarly, the intensity ratio at iris I2 (position D) of Figure 2.5, is;

$$\left(\frac{I}{I_0} \right)_2 = \frac{[1 - \sqrt{1 - (\delta_1/2R)^2}]}{[1 - \sqrt{1 - (\delta_2/2R)^2}]} \quad (2.4)$$

where δ_1 and δ_2 are the iris diameter, and the actual cross-sectional beam diameter, respectively. Noting that the new source point is located at position Z, the resulting intensity ratio is 62.33%.

The losses at the cylindrical lens positions are handled in a similar fashion. The intensity ratios are 5.95% and 74.0% for the first and second cylindrical lenses, respectively.

An account of efficiency due to reflection at each surface of uncoated lenses is given by;

$$r = 1 - \left(\frac{n - n_1}{n + n_1} \right)^2 \quad (2.5)$$

Since the index of refraction of glass relative to air is 1.5, $r = 0.96$. There is a total of five lenses in the light slicing system (three within the camera lens and 2 cylindrical lenses). This implies a total ratio of 0.96^{2n} , where n is equal to the number of lenses.

The mirror used behind the flash lamp effectively doubles the efficiency of the first stage, and therefore, the efficiency of the system.

An overall optical ratio for the light slicing system is now given by;

$$\left(\frac{I}{I_0}\right)_{total} = 2(0.96)^{2n} \left(\frac{I}{I_0}\right)_1 \left(\frac{I}{I_0}\right)_2 \left(\frac{I}{I_0}\right)_3 \left(\frac{I}{I_0}\right)_4 \quad (2.6)$$

For the arrangement given in Table 2.3, the efficiency is 0.0606%.

2.3.3 Available Power

The above analysis shows that the available power for visualization, using the single-shot 25 megawatt source, is approximately 150 Watts. This is about four orders of magnitude above the available light for a laser system costing about the same price.

2.4 Non-Optical Components

This section presents the various hardware used in the laboratory, that has not been described so far.

2.4.1 Shock Tube Design

An objective of this experimental investigation is the development of techniques to allow validation of CFD (computational fluid dynamic) codes. A key to achieving this objective is the definition and specification of identical boundary conditions for both the experimental and

computational investigations. To establish equivalent initial and boundary conditions, a shock tube is employed to produce the starting transient gas jet.

A 2.22 cm (7/8 inch) diameter shock tube with a 25.4 cm (10 inch) driver section and a 30.5 cm (12 inch) driven section has been constructed. The shock tube is shown in Figures 2.7 and 2.8. The shock tube was designed to permit flat shocks to develop prior to exit and to have an exhaust large enough for clean images to be made. The shock tube can be instrumented with pressure transducers along its length.

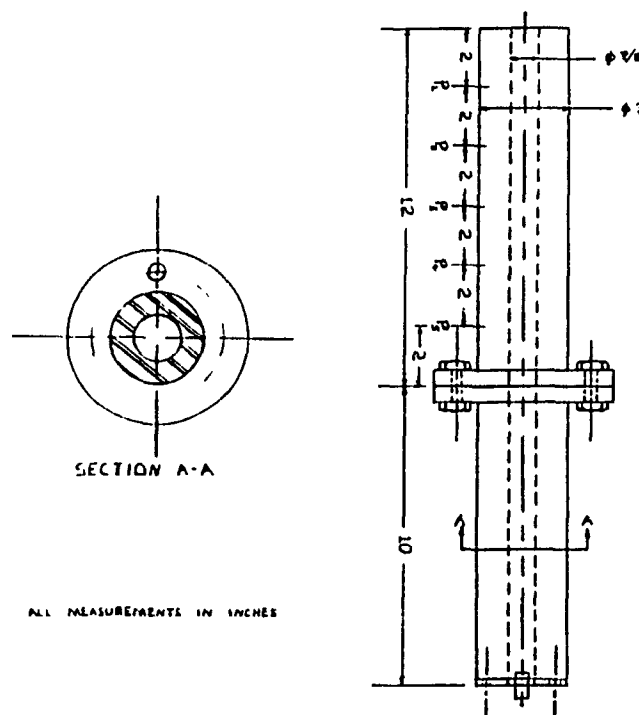


Figure 2.7 : Shock Tube

It is arranged vertically, with the open driven side up. This permits settling of smoke seed used in various experiments.

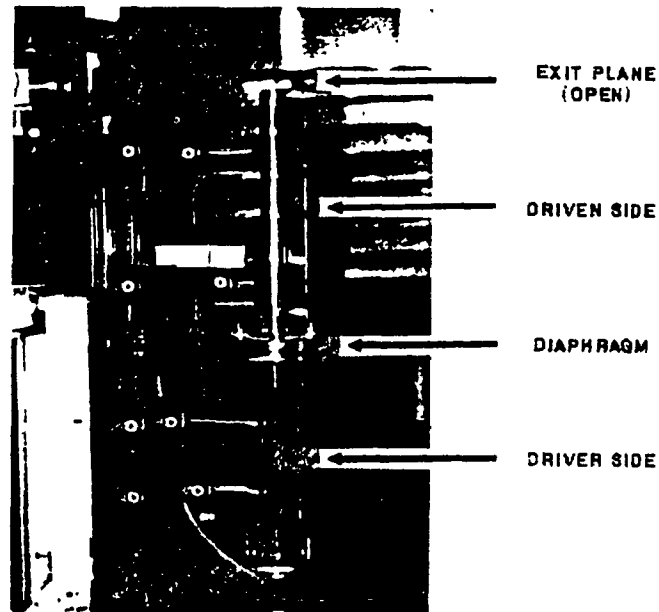


Figure 2.8 : 22 mm Diameter Shock Tube

The driven section gas is separated from the driver section gas by a 0.025 mm (0.001 inch) thick aluminum foil that bursts at a nominal driver pressure of 262 kPa (38 psig), i.e. when the $P_{\text{driver}} / P_{\text{driven}}$ pressure ratio is about 3.58.

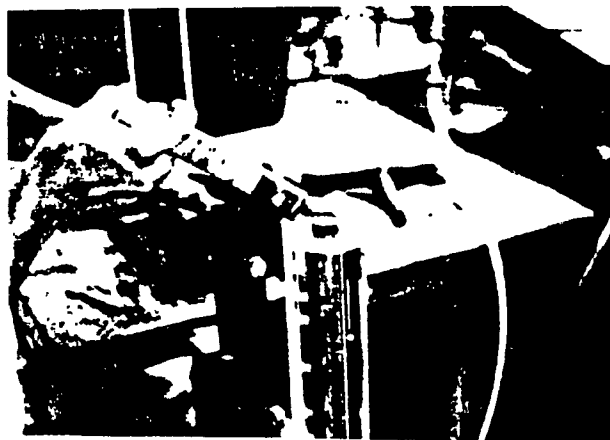
The shock tube has been chosen as the transient jet simulator so that there would be no discrepancies in initial conditions. Any nonuniformities in the breaking of the diaphragm eventually average out by the time the flow reaches the exit.

The driven section gas is air in the schlieren system, and a mixture of air and smoke in the light slicing system.

Approximately 75 cc of tobacco smoke is used as the scattering medium in the flash lamp light slicing technique. Smoke via syringe as shown in Figure 2.9 is driven from a cigar and injected. Smoke particle size is of the order of $1 \mu\text{m}$.



(a) Driving smoke



(b) Injecting smoke

Figure 2.9 : Driving and Injecting Smoke

2.4.2 Test Gases

In order to investigate mixing phenomena of starting jets globally, it was originally intended to study three different gases of molecular weight (MW) ratios (relative to air) of 0.1, 1.0, and 10.0. For that purpose, Sulfur hexafluoride, SF₆, with a MW ratio of 5.04 was considered for the heavier gas. However, investigation showed this to be an asphyxiant, unsuitable for use in our facility, and was abandoned as a test case. Helium (MW ratio 0.138) was chosen as the lighter test gas.

Due to the nature of the experiments there is always air along with the test gas used in the driven section of the shock tube. Nevertheless, this is neglected for identifying experimental cases.

2.4.3 Electronics

Shock tube instrumentation and timing systems are shown in Figures 2.10 and 2.11. The shock tube can be instrumented with piezoelectric pressure transducers located at feed throughs along its length. Each feed through has a 1 mm diameter port to the flow section of the shock tube. The pressure transducers are PCB Piezotronics pressure transducers modules 112A with a rise time of 2 microseconds and a

resolution of 400 Pa. The pressure transducer signal is amplified (by a PCB Piezotronics model 462A charge amplifier) monitored an IWATSU Model SS-5802 digital storage oscilloscope and used to trigger a programmable delay timer.

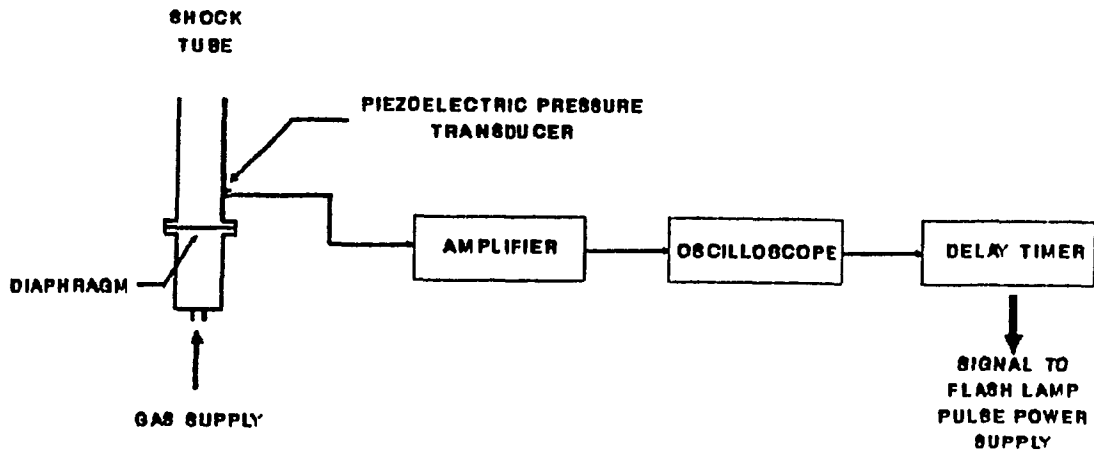


Figure 2.10 : Instrumentation and Timing System

The programmable delay timer has been designed and built in order to assure the accuracy of the timing between the shock tube burst and the flashing of the lamp. The timer can be programmed for delays of 0.1 μs to 9999.9 μs following receipt of a trigger signal of 0.3 Volts.

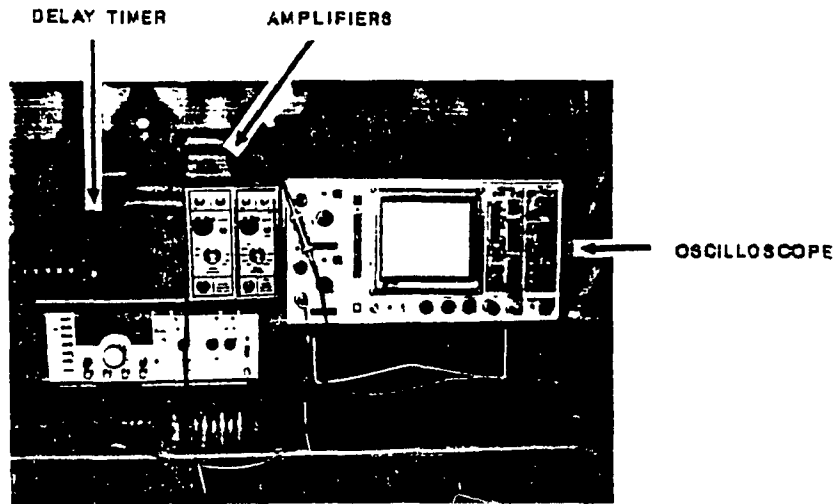


Figure 2.11 : Photograph of Instrumentation and Timing System

A block diagram of the delay timer is shown in Figure 2.12. Triggering is accomplished by applying a rising edge signal, either analogue or digital, to the input port. The timer then counts down until the delay set on the front panel thumb wheels is reached. Given identical input trigger pulses for two separate events, the worst case delay to acknowledge one trigger with respect to the other is 100 ns. That is, the second output leads or lags the first output by at most 100 ns. This implies an accuracy of 200 ns of the dial setting. This is presumed negligible for the time scale of the experimental trials.

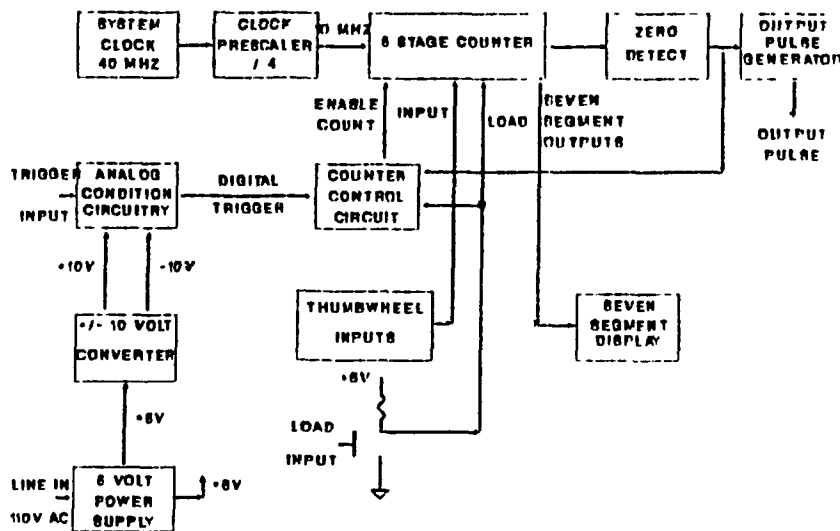


Figure 2.12 : Delay Timer Block Diagram

The delayed signal from the timer is sent to the flash lamp electronic assembly, shown in Figures 2.13 and 2.14.

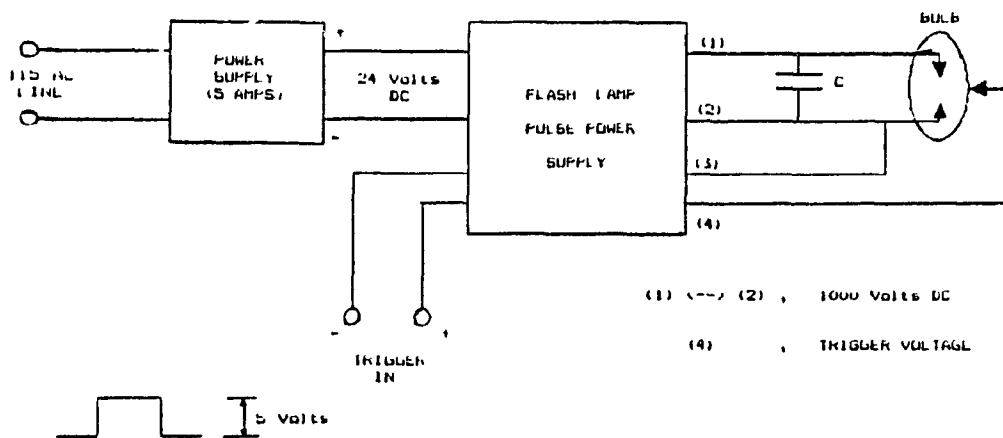


Figure 2.13 : Flash Lamp Electronic Assembly

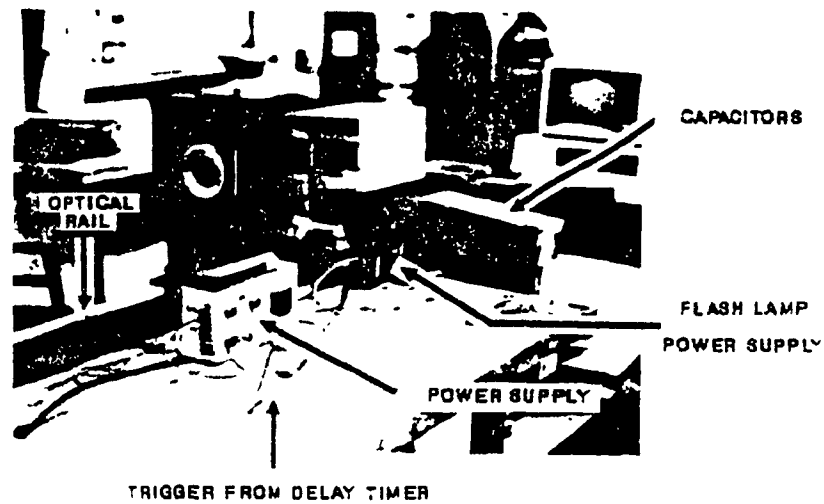


Figure 2.14 : Photograph of Flash Lamp Electronic Assembly

2.4.4 Camera and Film

The camera employed is a Linhof Techniks 4X5 large format camera with a Schneider Xenar 150 mm, f4.5 lens. The camera is mounted on a Bilora 3124-1462 tripod and head for light slicing, or on an optical rail for schlieren work. For immediate results, a Polaroid (TM) pack and Polaroid Type 667 film are utilized.

Due to the scattering properties of smoke particles [Ref. 11], the camera was positioned at an angle to the flow axis. This is shown in the axial light slicing set-up of Figure 2.15, and the transverse light slicing set-up of Figure 2.16.

Note that, the object plane in Figure 2.15 is perpendicular to the shock tube exit plane, whereas, the object plane in Figure 2.16 is parallel to the exit plane.

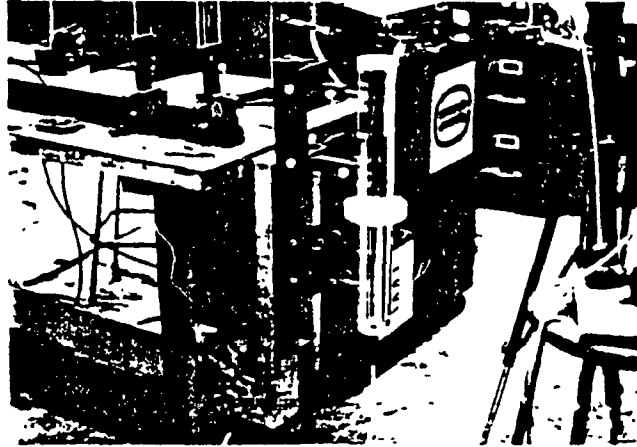


Figure 2.15 : Axial Light Slicing Setup



Figure 2.16 : Transverse Light Slicing Setup

When attempting to photograph objects at an angle, that is with a view other than perpendicular to the object plane, the image plane has to be oriented to be sharp over the entire field. The relationship between the view plane and the image plane is described by the Scheimpflug rule of intersecting planes; as mentioned earlier, the resulting image does not have uniform magnification. Section 3.1 shows the relation between a point on the photograph, and an actual position on the jet.

2.5 Accuracy of Systems

One of the most demanding criteria in the experiments is the reproducibility of the results. To that end, the shock tube diaphragm burst pressure was investigated and although not always consistent, shock velocity, as measured by the time difference for shock arrival between two transducers, and appearance of the wrinkles and tears in the broken diaphragm is observed to correlate with the driver pressure and the form and time of shock exit from the tube.

Two systems were used. First, as shown in Figure 2.17, the approximate burst pressure is measured using the "Lazy Hand" Bourdon gauge, connected in the gas feed line of the driver section of the shock tube. Then, since the signal from a pressure transducer on the driven side is monitored by the

oscilloscope, it is also used as verification. Note that, the consistency of the signal from the pressure transducer is deemed more important than correlation with the pressure gauge measurement.

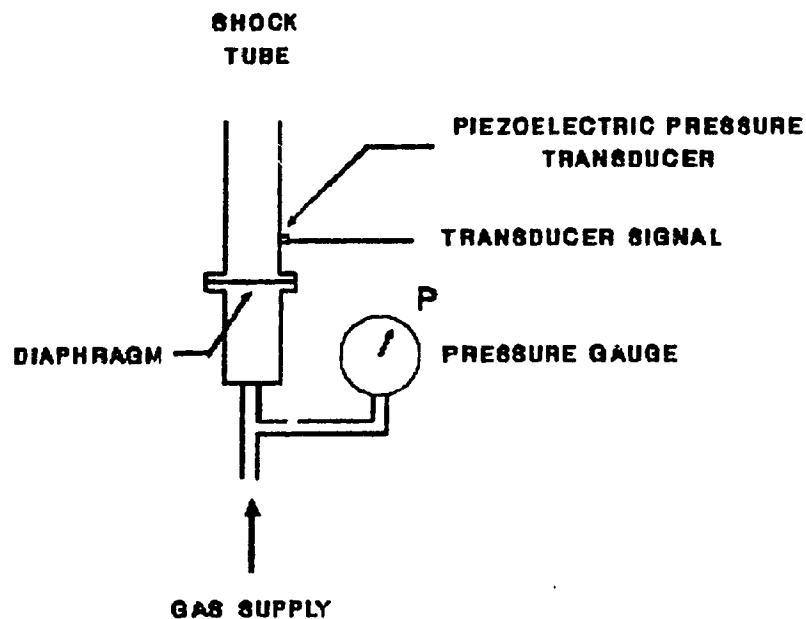


Figure 2.17 : Pressure Measurement Systems

A statistical account of the shock tube burst pressure based on correlation with results was considered. Using the timer set at a fixed delay, the on-axis extent of the jet was measured from the photographic results for repeated bursts. Twenty five bursts, and thus 25 pictures of air driving air and smoke in the light slicing technique were taken.

The pressure transducer signal was found to have a linear correlation with the downstream axial distance. However, the

results show that it was reasonable to restrict the feedback pressure such that the error in linear distance of the jet was ± 1 mm.

The error mentioned above was held for air driving air and smoke in the light slicing technique. Other experimental runs were not as restrictive in the feedback pressure, and therefore not as accurate. For this reason only confidence intervals are provided in the various quantitative results to follow. The magnitude of the "confidence error bar" is assumed to be one radius.

2.6 Effect of Smoke

Tobacco smoke was used as a light scattering medium in various experiments. However, questions arise about the ability of the smoke tracers to follow the flow. The simple exercise of Merzkirch, leads us to understand that in order to know the drag of the smoke particles in particular flow situations, a solution of the Navier-Stokes equations is required [Ref. 12]. It is important to note however, that the smaller the particle size, the less effect it will have on the fluid. Yet, the question of how closely the smoke particles follow the flow, remains unanswered.

The effect of smoke is neglected in the analysis of the following chapters.

3.0 EXPERIMENTAL RESULTS

Photographic results from both schlieren and light slicing flow visualization of starting gas jets are presented in this section. Trials were conducted for both air and helium driving mixtures of air and smoke into the atmosphere, using the shock tube apparatus. Images in each series of shock tube discharges were taken at 20 μ s intervals. This corresponds to 50,000 frames per second. However, only intervals of 80 μ s are presented here. Complete results with original photographs are given in Reference 13.

3.1 Data Reduction

Figure 3.1 shows a typical axial light slicing result for a vertical discharge from the shock tube. The head of the jet can be observed to have a "mushroom" shape, while the core is bordered by curls of gas. In order to decode the final results from the photograph, a mathematical transformation is required. The transformation relates co-ordinate positions on the photograph to actual positions on the jet.

The view of the jet in this photograph is distorted in a number of ways: First, the magnification on axis is about 0.66. Second, because the camera is positioned at a scattering



Figure 3.1 : Axial Light Slicing Result

angle, the jet appears compressed to the left of its centre-line and expanded on the right. Both axial and transverse results correspond to a scattering angle of 52 degrees. Third, the light scattering angle causes a perspective projection from top to bottom of Figure 3.1. The angle of the perspective view is estimated from the results. Forth, since the camera is aimed approximately 50 mm above the jet exit in the axial experiments, there is a perspective view from left to right. However, this is neglected since the view width is smaller than its length.

The scattering angle effect is considered in Figure 3.2. The figure shows the object plane, lens plane and image plane for a camera setup. Only the light rays passing through the

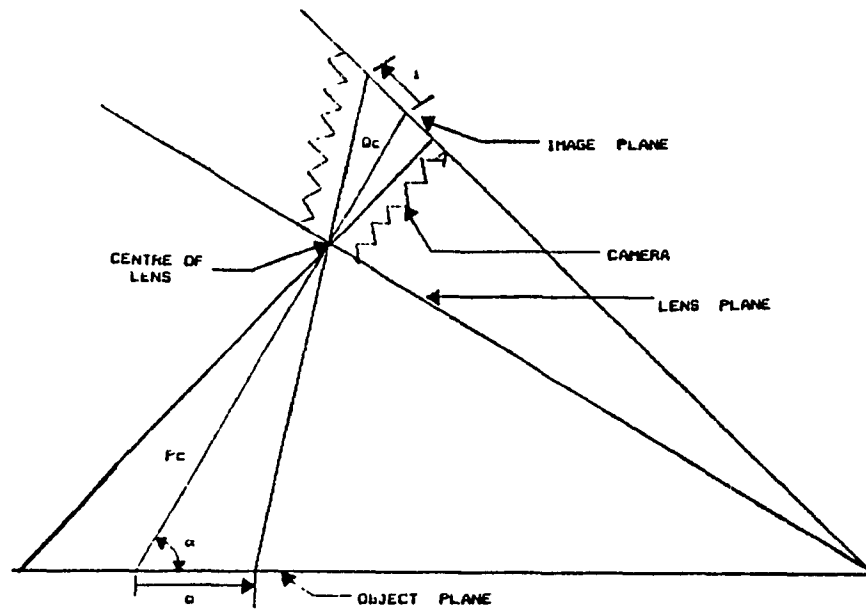


Figure 3.2 : Scattering Angle Effect

centre of the lens are considered. When the scattering angle, α , central-axis magnification, M_c , and focal length, f , of the camera lens are known, the image distance, i , becomes a function of object distance, o , alone. This is described by:

$$i = [Q_c^2 - 2Q_o c \cos(\beta) + Q^2]^{1/2} \quad (3.1)$$

where,

$$Q = \frac{f [P_c^2 - 2P_c o \cos(\alpha) + o^2]^{1/2}}{[P_c^2 - 2P_c o \cos(\alpha) + o^2]^{1/2} - f} \quad (3.2)$$

and,

$$\beta = 90 - \alpha - \tan^{-1} \left[\frac{P_c \cos(\alpha) - o}{P_c \sin(\alpha)} \right] \quad (3.3)$$

Note that P_c and Q_c are obtained as follows;

$$P_c = f \left(\frac{1}{M_c} + 1 \right) \quad (3.4)$$

$$Q_c = P_c * M_c \quad (3.5)$$

Now, the axial light slicing result is repeated in Figure 3.3 along with a grid that incorporates the geometrical transformation discussed above. The grid is used as a

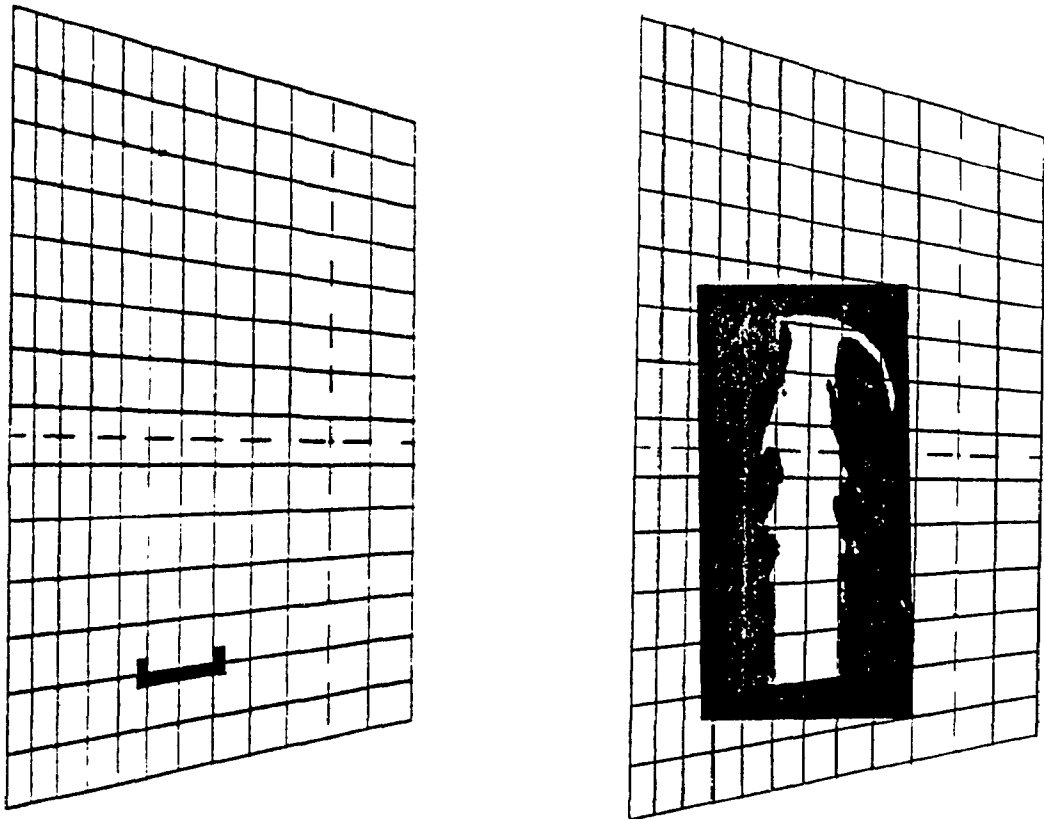



Figure 3.3: Axial Light Slicing Result with Data Reduction Grid

graticule to obtain quantitative data from the pictures. Each grid on the figure is equivalent to a torus with a square cross section on the actual jet. The intersection of the dotted lines on the grid represents the centre of the camera lens and symbol  is the shock tube exit plane.

3.2 Axial Results

The schlieren and light slicing set-ups were used to photograph the starting jet in the axial direction, that is, where the optical view was perpendicular to the flow direction.

3.2.1 Schlieren

Three sets of schlieren photographs of shock tube discharges have been taken. Two are presented in this section: Helium driving air into ambient air, and air driving air into ambient air.

3.2.1.1 Helium Driving Air

Helium driving air into air is illustrated in Figure 3.4. The convex shock wave emerges from the shock tube approximately 400 μ s after the electronic sequencer is



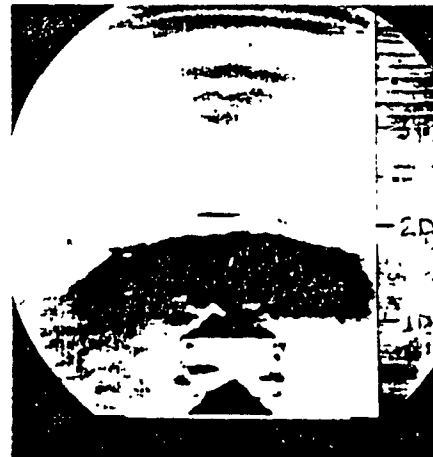
(a) 20 μ s



(d) 260 μ s



(b) 100 μ s



(e) 340 μ s



(c) 180 μ s



(f) 420 μ s

Figure 3.4 : Schlieren - He driving Air (...continued)



(g) 500 μ s



(i) 660 μ s



(h) 580 μ s



(j) 740 μ s

Figure 3.4 : Schlieren - He driving Air

triggered by a pressure transducer signal. This is chosen to be the time datum.

The photographs show the formation of the exit vortex. This vortex grows throughout the sequence shown here. Photographs (b) to (g) clearly show the formation of Mach diamonds behind the head of the wave.

There is some question about the position of the interface between the shock treated ambient gas and the driven gas. It is not to be confused with the interface between the driver and driven gases.

Photographs (g) to (j) of Figure 3.4 shows the break-up of the Mach diamond structures. By photograph (j), 740 μ s after the shock has emerged from the exit, the overall flow seems to be on its way to steady state conditions.

3.2.1.2 Air Driving Air

Air driving air into air is illustrated in Figure 3.5. Again, when the shock wave emerges from the shock tube, at about 540 μ s time is set at 0.0 sec datum. The scale in this illustration is the same as that of Figure 3.4.



(a) 20 μ s



(d) 260 μ s



(b) 100 μ s



(e) 340 μ s



(c) 180 μ s



(f) 420 μ s

Figure 3.5 : Schlieren - Air driving Air (...continued)



(g) 500 μ s



(i) 860 μ s



(h) 580 μ s

Figure 3.5 : Schlieren - Air driving Air

Photograph (a) shows the emergence of the shock wave from the exit plane of the shock tube, as well as the initiation of the vortex ring structure. Again the vortex ring grows steadily throughout the sequence.

By photograph (d) of Figure 3.5 a "cork-screw" like structure seems to be present on the stem of the jet, in photographs (d) through (i). This may signify that the entire three-dimensional structure may be rotating as it develops. However, unlike the earlier He driving case no Mach diamonds are observed.

Closer examination of these pictures reveals a region above the head of the vortex ring that is brighter than the background. At this time we believe that the top of this bright region is the interface between the driven gas and ambient air. This is clearly illustrated in photographs (f) and (g).

3.2.2 Light Slicing

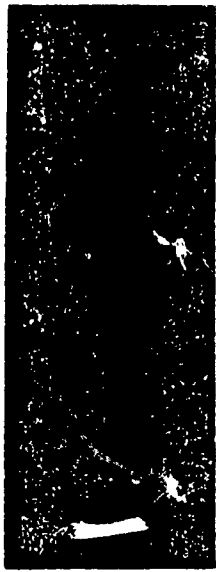
As mentioned in earlier sections, smoke was used to provide light scattering particles for light slicing. The resulting photographs do not show an initial shock wave, as in schlieren, due to the nature of the experiment.

The fluid lamina photographed within the three-dimensional jet reveal complex internal structures not observed in schlieren. These are deemed "coherent structures" [Ref. 14].

3.2.2.1 Helium Driving Air + Smoke

Light slicing results of helium driving air and smoke into air is illustrated in Figure 3.6. Photograph (a), at 20 μ s, shows the start of the vortex; the vortex again grows throughout the sequence given here. By photograph (d) of Figure 3.6, 260 μ s after the vortex has emerged from the shock tube exit, "feather-like" structures have formed where the main vortex head has curled back to the shaft of the flow. These structures spread as the flow moves away from the shock tube exit plane. Photographs (f) to (j) show that these "feather-like" structures progress and develop into turbulence along the shaft of the main flow.

Close examination of many of these photographs, reveals Mach diamond patterns in the shaft of the main flow, as has been observed in the schlieren results.



(a) 20 μ s



(b) 100 μ s



(c) 180 μ s



(d) 260 μ s



(e) 340 μ s



(f) 420 μ s



(g) 500 μ s



(h) 580 μ s

Figure 3.6 : Light slicing - He driving Air+smoke(..continued)



(1) 660 μ s

(2) 740 μ s

Figure 3.6 : Light slicing - He driving Air+smoke

3.2.2.2 Air Driving Air + Smoke

Air driving air mixed with smoke into air is illustrated in Figure 3.7. The "feather-like" structures again are present approximately 260 μ s after the vortex emerges from the shock tube exit. As observed before, these features spread as the flow progresses.

These "feather-like" features develop into distinct coherent structures by photograph (f) of Figure 3.7. These structures continue to develop in photographs (g) and (h), until they seem to breakup by photographs (i) and (j). It is noted here that the structures are not symmetric about the centre line. Instability in the flow field may be the reason for non-symmetry and eventual breakup of these structures [Ref. 15].

It must be noted here that the helium driving air and smoke series does not have the distinct coherent structures observed in Figure 3.7. This may be due to the Mach diamond interactions present in the flow of Figure 3.6.



(a) 20 μ s



(b) 100 μ s



(c) 180 μ s



(d) 250 μ s



(e) 340 μ s



(f) 420 μ s



(g) 500 μ s



(h) 530 μ s

Figure 3.7 :Light slicing - Air driving Air+smoke(..continued)



(1) 660 μ s



(2) 740 μ s

Figure 3.7 : Light slicing - Air driving Air+smoke

3.2.3 Schlieren - Air Driving Air + Smoke

A quick comparison of the schlieren and light slicing images reveal that it is difficult to distinguish between the vortex ring observed from schlieren, and the vortex from light slicing. To resolve the issue, it was decided to carry out an additional series of schlieren studies involving visualizing air driving air and smoke, into ambient air. Results are illustrated in Figure 3.8. In photograph (b), 100 μ s after the shock emerges, two distinct structures are observed behind the shock wave. The first is the vortex structure appearing in the light slicing photographs, while the second is the vortex ring that the schlieren photographs of air driving air into air reveal. We call the light slicing vortex, a "primary vortex", and the schlieren vortex the "vortex ring".

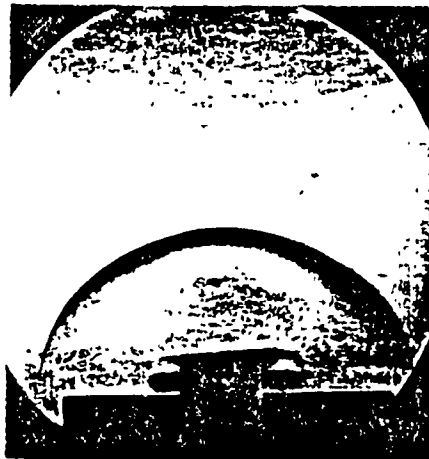
Figure 3.9 defines the flow regions present in the starting jet. First, the shock wave appears. Then, the primary vortex. This is followed by the vortex ring at the base of the primary vortex. The core flow, behind the vortex ring is bounded by non-symmetric coherent structures. It is important to note that the vortex ring appears mounted on the primary vortex. That is, the vortex ring always lies at the bottom of the primary vortex. There is also the possibility that the primary vortex "feeds" the vortex ring during its growth.



(a) 20 μ s



(d) 260 μ s



(b) 100 μ s



(e) 340 μ s



(c) 180 μ s



(f) 420 μ s

Figure 3.8: Schlieren - Air driving Air+Smoke

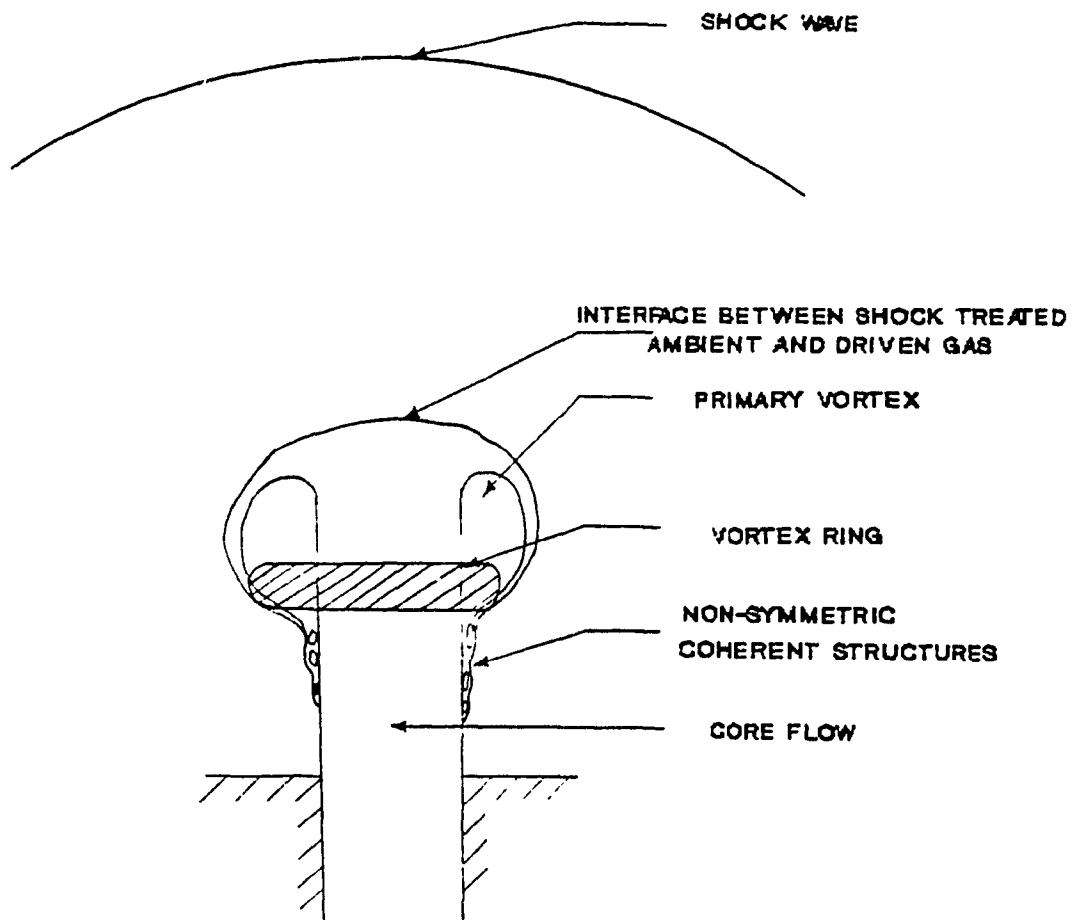


Figure 3.9: The Starting Jet

It is now clear that the interface between the shock treated ambient gas and the driven gas is the top of the primary vortex and not the top of the vortex ring, as was suggested from the initial schlieren results.

3.2.4 Quantitative Results

Five variables have been measured from the photographic data. These are defined in Figure 3.10. They are:

- 1) Shock Extent
- 2) Vortex Ring Extent
- 3) Primary Vortex Extent
- 4) Left Primary Vortex Width
- 5) Right Primary Vortex Width

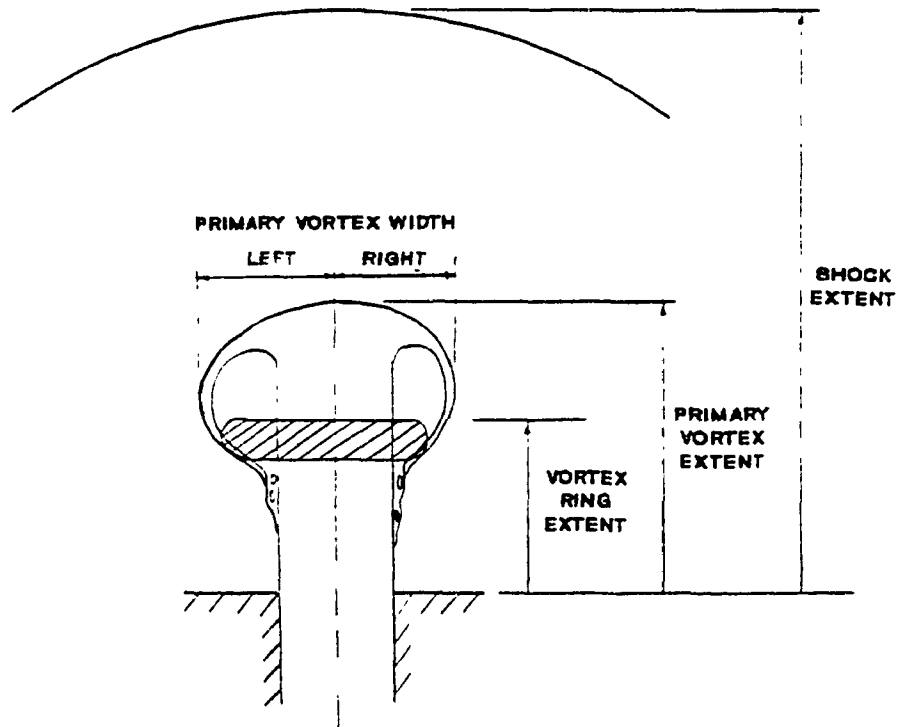


Figure 3.10: Quantitative Measurements

The first two are measured from the schlieren results, while the primary vortex data is obtained from the light slicing photographs. Figure 3.11 shows the position of the primary vortex as a function of time. It compares the primary vortex

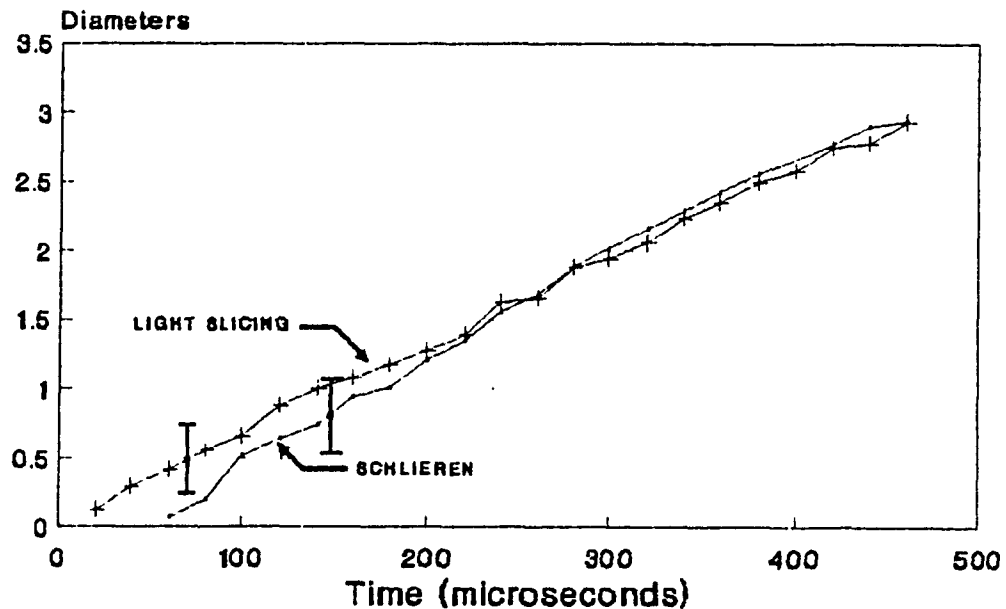


Figure 3.11: Comparison of Primary Vortex Extent

extent obtained from the two photographic results of air driving air and smoke (ie. schlieren and light slicing). This exercise confirms the repeatability of the results and validates the data reduction grid obtained in Section 3.1. In this figure, the vertical bar indicates the confidence interval which was defined above as one radius in magnitude.

Figures 3.12 and 3.13 illustrate the variation of the shock, vortex ring, primary vortex extent and width for an air (and smoke) gas jet generated with a helium driver. The figures also show the results of one dimensional shock tube theory calculations. A constant shock velocity of 513.6 m/s has been calculated as shown in Figure 3.12. The difference

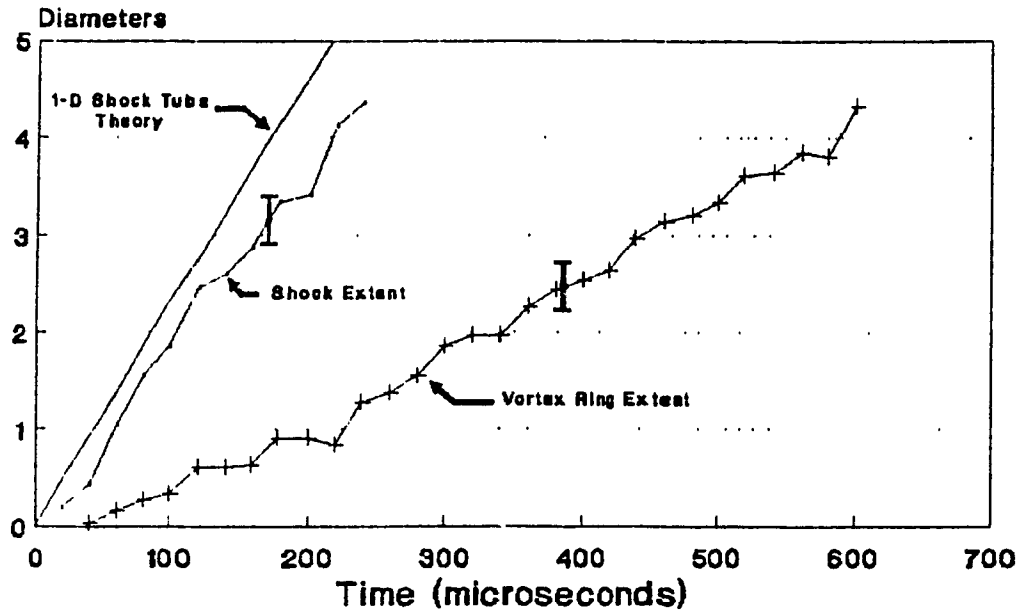


Figure 3.12: Schlieren Data: Helium driving Air

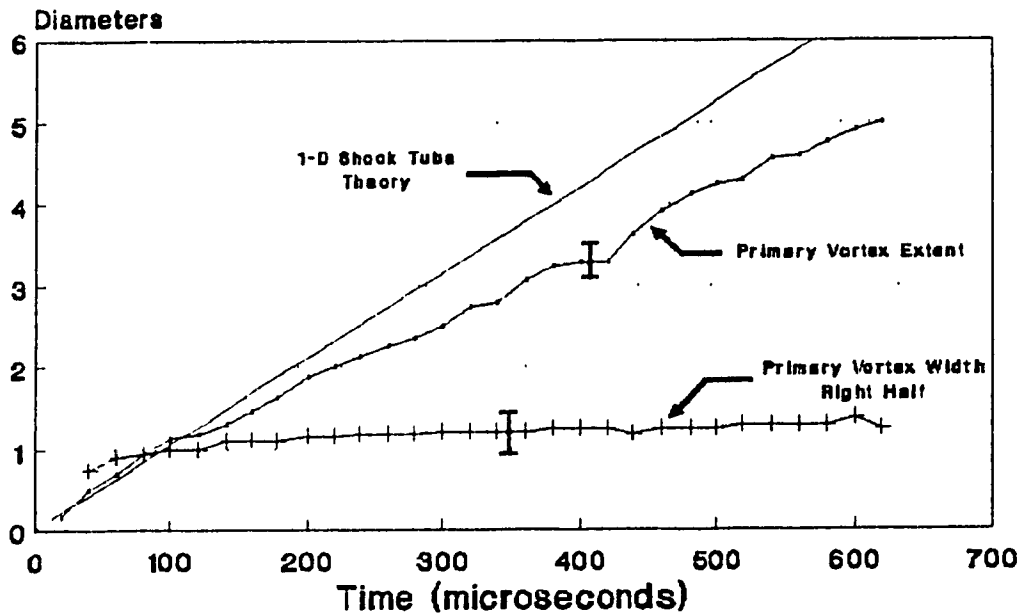


Figure 3.13: Light Slicing Data: He driving Air+Smoke

between this value and the shock extent data is due to the amount of energy transferred in the other two dimensions as the jet develops radially. The same applies in Figure 3.13 where a constant velocity of 233.7 m/s is given for the driven gas. The effect of the smoke particles in the driven gas is neglected. It should be noted that one dimensional shock tube theory holds within the shock tube. The distance between the pressure transducer feed through and the exit of the nozzle divided by the time datum delay given from the electronic sequencer is identical to the theoretical shock velocity.

Similar data are given in Figures 3.14 and 3.15 for air driving air (and smoke). The theoretical shock velocity and driven gas velocity are 453.3 m/s and 157.6 m/s respectively. Again the effect of the smoke particles is neglected. The one dimensional theoretical solution is closer to the measured data in this case.

The shock, primary vortex and vortex ring extent derived from schlieren data are all given in Figure 3.16, for air driving air+smoke. This illustrates the data derived from the photographs shown in Figure 3.8.

Assuming the data presented so far are linear gives approximate velocities listed in Tables 3.1 and 3.2. These tables also show the comparison between the photographic

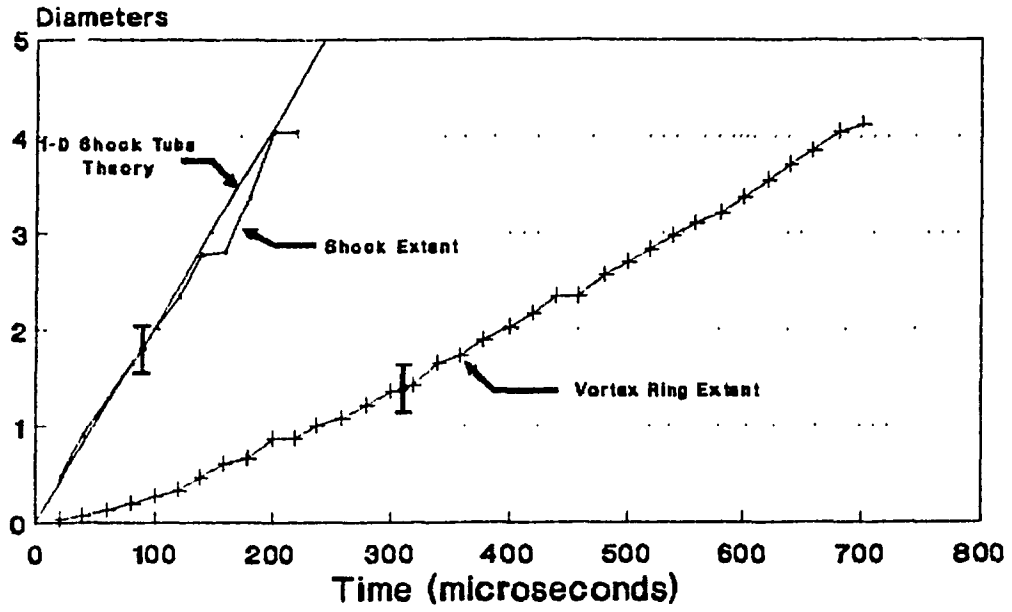


Figure 3.14: Schlieren Data: Air driving Air

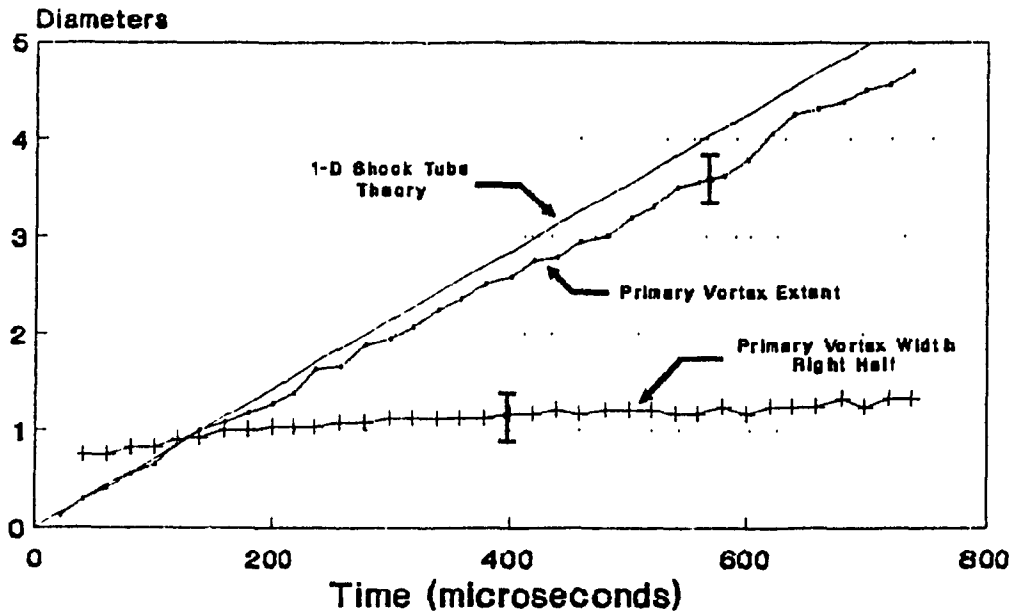


Figure 3.15: Light Slicing Data: Air driving Air+Smoke

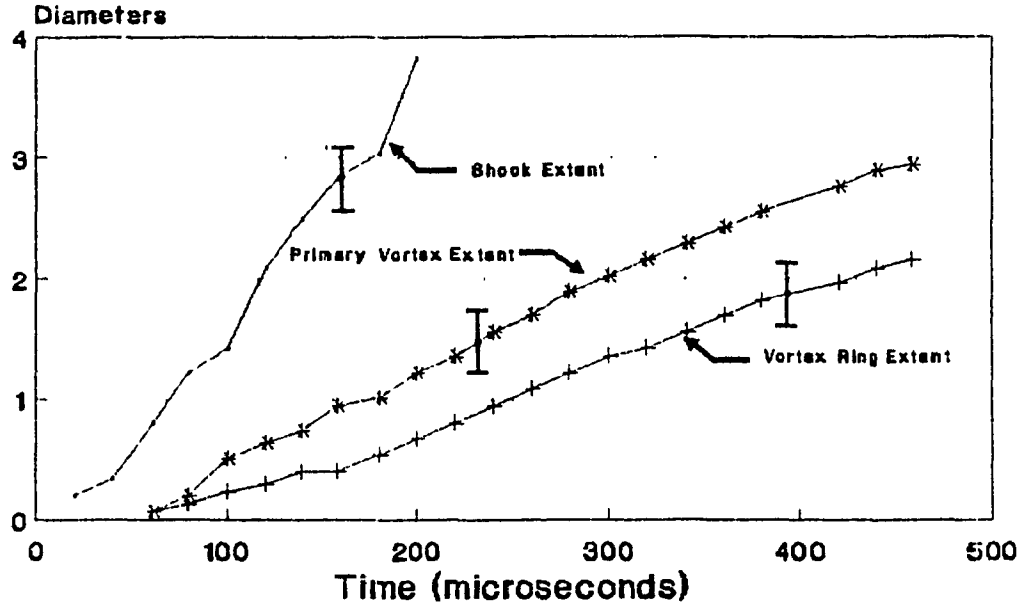


Figure 3.16: Schlieren Data: Air driving Air+Smoke

RESULTS FROM VARIABLE	1-D SHOCK TUBE THEORY	SCHLIEREN	LIGHT SLICING (+ SMOKE)	SCHLIEREN (+ SMOKE)
SHOCK	453.3	402	—	419
VORTEX RING	—	139	—	124
PRIMARY VORTEX	157.6	—	141	163

Table 3.1: Air Driving Air (Velocities in m/s)

RESULTS FROM VARIABLE	1-D SHOCK TUBE THEORY	SCHLIEREN	LIGHT SLICING (+ SMOKE)
SHOCK	513.5	417	—
VORTEX RING	—	169	—
PRIMARY VORTEX	233.7	—	175

Table 3.2: He Driving Air (Velocities in m/s)

results and the one dimensional shock tube theory. We note that the helium driver causes larger deviations between the 1-D shock tube theory, and the light slicing and schlieren measurements than is the case for the air driver.

3.3 Transverse Light Slicing Results

In addition to the axial light slicing series, transverse light slice visualization has been undertaken for air driving air and smoke into the atmosphere. The transverse images have been recorded at approximately 1, 2, 3, 4 and 6 diameters downstream from the exit of the shock tube. Diameters 1 through 4 are presented here.

3.3.1 Air Driving Air + Smoke

The transverse light slicing results are summarised in Figure 3.17. Again, the time interval between images is $80 \mu\text{s}$. Reference 13 has complete results. For completeness axial results accompany Figure 3.17.

At $160 \mu\text{s}$ after the primary vortex emerges from the shock tube exit, photograph (a), the head of the vortex reaches one diameter. Photograph (b) shows a double ring structure, this structure is approximately one diameter away from the nozzle exit. This structure is approximately centered on the primary vortex observed in the axial light slicing photograph.

At $320 \mu\text{s}$ into the flow the jet has progressed more than two diameters axially from the shock tube exit plane. At this time, the primary vortex has curled back into the stem of the jet at the one diameter axial location. From the one diameter downstream image at $320 \mu\text{s}$, it appears that there is a circumferential asymmetry that suggests a circumferential component of velocity in the jet. This may again signify that the jet is rotating as it develops.

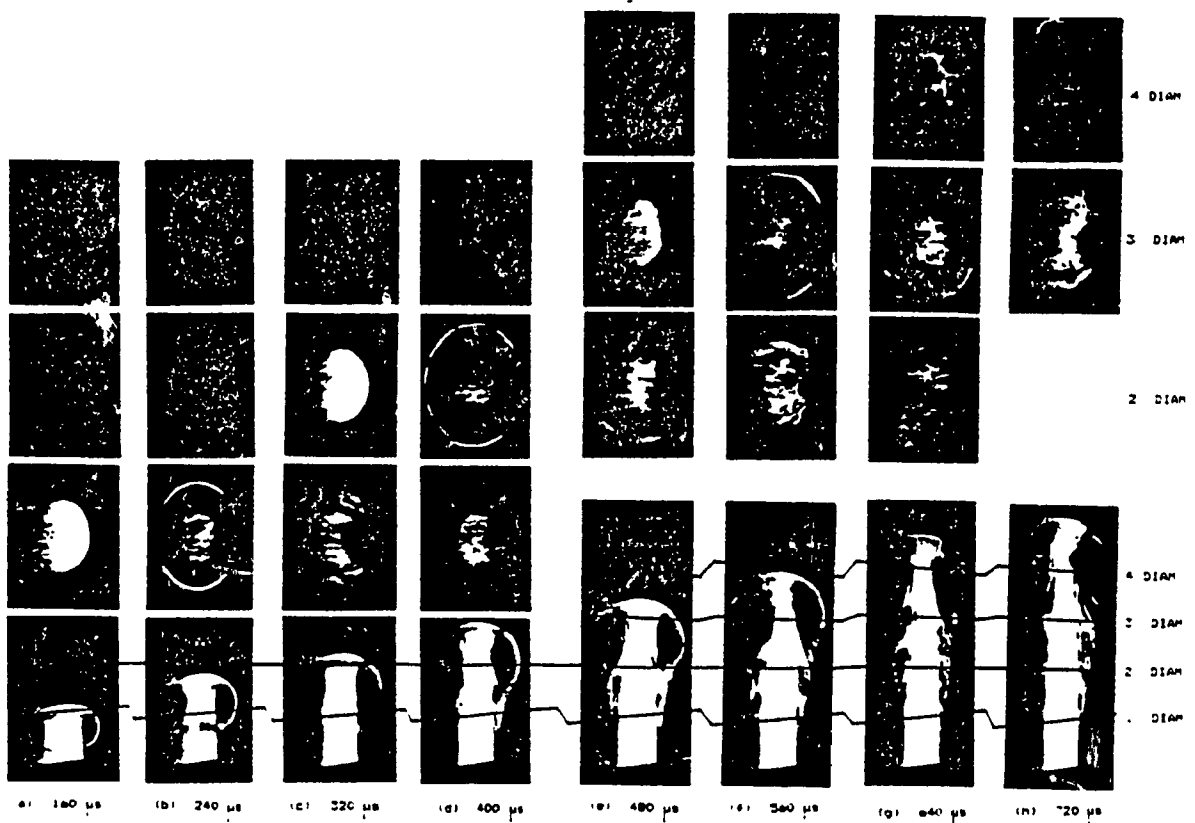


Figure 3.17: Transverse Light Slicing Results:
Air driving Air+Smoke

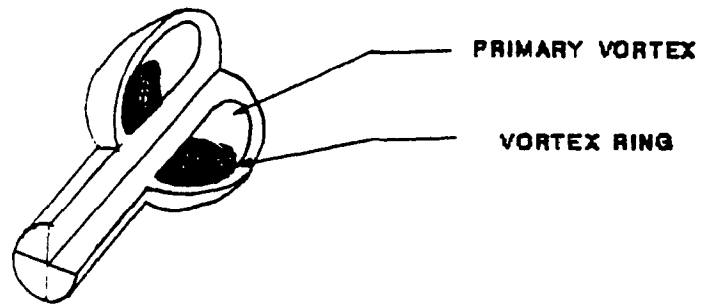
It should be noted at this point that up to approximately 240 μ s into the flow, i.e. one and a half diameters, the jet seems to be axisymmetric.

In photograph (d), 400 μs after the vortex emerges from the shock tube exit, distinctly three dimensional effects are present; at two diameters, both the inner and outer ring structures are non-symmetric. By photograph (g), 640 μs , it is clear that the non-uniformity in the transverse light slicing results suggest that what may be an initially axysymmetric starting jet develops a number of three-dimensional lobes. This is shown at 640 μs , for two and three diameters, where five lobes appear. The inner core ring is less straight forward to interpret. Many voids appear in the inner ring. At two-diameters, approximately 9 lobes seem to join with the outer ring, forming coherent structures as shown in the axial result of photograph (g).

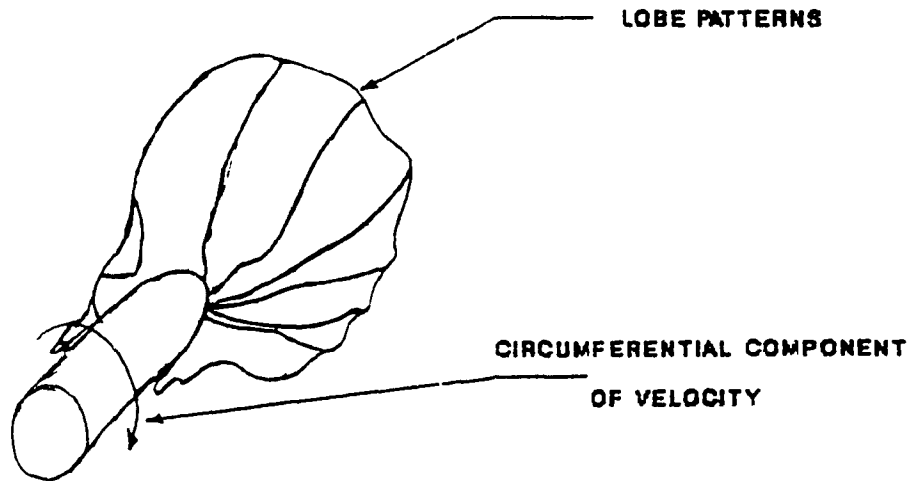
3.4 Three-Dimensional Integration

Figure 3.18 shows a conceptual reconstruction of the three-dimensional effects present in the starting jet. This figure is obtained by combining the axial and transverse light slicing results. At 240 μs after the emergence of the vortex, the jet is still axisymmetric and homogeneous. It has progressed approximately 1 and 3/4 diameters. At 640 μs the jet front is approximately 4.5 diameters downstream. Distinct three-dimensional effects are present such as five

circumferential lobes on the surface of the jet. A circumferential component of velocity is also shown.



(a) 240 μ s



(b) 640 μ s

Figure 3.18: 3-D Reconstruction of Starting Jet:
Air driving Air+Smoke

4.0 CONCLUDING REMARKS

Schlieren and light slicing have been used to visualize the starting gas jet. The light slicing method developed here is shown to be a cost effective means for visualizing the inner structure of the gas jet.

Although many results have been presented at relatively high Reynolds and Mach numbers, compared to other investigations in the literature, the question of the ability of the smoke particles to follow the flow remains moot.

Discrete flow regions have been identified in the starting jet including secondary flow effects. These effects include "cork-screw" and Mach diamond structures at the stem of the jet, and three dimensional coherent structures.

4.1 Future Work

The photographic results presented in this thesis should be compared to other experimental photographic results for different Reynolds numbers. This would identify the value of the incompressible numerical model presented here as a representation for the experimental work.

Additional photographic studies could include comparison of schlieren images taken with and without smoke tracers. This may signify how close the smoke particles follow the flow.

The experimental results presented here could have been more accurate by further classifying the results based on the pressure transducer signals.

An alternative to the present experimental techniques would be to design and employ a system where one shock tube burst would result in multiple photographic results.

LIST OF REFERENCES

Chapter 1: INTRODUCTION

1. Rogers, W.B., "On the formation of rotating rings by air and liquids under certain conditions of discharge", American Journal of Science and Arts, 26 (1858)
2. Czermak, P., "Eine Neue Beobachtungsmethode fur Luftwirbelringe", Weimer Berichte, 109, IIa (1900)
3. Indra, A., Weiner Berichte, 110, IIa (1901)
4. Johansen, F.C., "Flow through pipe orifices at low Reynolds numbers", Proceedings of the Physical Society, Volume 126, 1929, pp. 231-245.
5. Hussain, A.K.M., "Coherent Structures and Turbulence", Journal of Fluid Mechanics, Volume 173, 1986, pp.303-356.
6. List, E.J., "Turbulent Jets and Plumes", Annual Review of Fluid Mechanics, Volume 14, 1982, pp. 189-212.

Chapter 2: EXPERIMENTAL METHODS

7. Kock, C., Marchesi, J.J., Photo Know-How, Sinar Ltd, Schaffausen, Feuerthalen, Switzerland, 1983, pp. 129-136.
8. Saber, A.J., "Study of Transient Jet Gases, Final Report", prepared with respect to DSS File Number-01SG.97702-R-5-0682, Concordia University, Montreal, Quebec, 1988 March 31, pg.98.
9. Saber, A.J., "Light Slicing for Observation of Fluid Flows", Applied Optics, Volume 25, Number 24, December 15, 1986, pp.4605-4608.
10. Saber, A.J., "Study of Transient Jet Gases, Final Report", prepared with respect to DSS File number- 01SG. 97702-R-5-0682, Concordia University, Montreal, Quebec, 1988 March 31, pg. 55.
11. van de Hulst, H.C., Light Scattering by Small Particles, Dover Publications, New York, NY, 1981, pp.115-227.
12. Merzkirch, W., Flow Visualization, Academic Press, New York and London, 1974, pp.21-27.

Chapter 3: EXPERIMENTAL RESULTS

13. Saber, A.J., "Study of Transient Jet Gases, Final Report", prepared with respect to DSS File Number-01SG.97702-R-5-0682, Concordia University, Montreal, Quebec, 1988 March 31, pp.155-294.
14. Hussain, A.K.M., "Coherent Structures and Turbulence", Journal of Fluid Mechanics, Volume 173, 1986, pp. 303-356.
15. Chandrasekhar, S., Hydrodynamic and Hydromagnetic Stability, Dover Publications Inc. New York, 1981, pp.428-463.